Cylindrical polymer brushes-anisotropic unimolecular micelle drug delivery system for enhancing the effectiveness of chemotherapy

Shuang Bai [a,c], Die Jia [a,c], Xianbin Ma [a,c], Mengyun Liang [a,c], Peng Xue [a,c], Yuejun Kang [a,c], Zhigang Xu [a,b,c,*]

[a] Key Laboratory of Luminescence Analysis and Molecular Sensing (Southwest University), Ministry of Education, School of Materials and Energy, Southwest University, Chongqing, 400715, PR China
[b] State Key Laboratory of Molecular Engineering of Polymers, Fudan University, Shanghai, 200438, China
[c] Chongqing Engineering Research Center for Micro-Nano Biomedical Materials and Devices, Southwest University, Chongqing, 400715, PR China

ARTICLE INFO

ABSTRACT

Polymer systems can be designed into different structures and morphologies according to their physical and chemical performance requirements, and are considered as one of the most promising controlled delivery systems that can effectively improve the cancer therapeutic index. However, the majority of the polymer delivery systems are designed to be simple *spherical* nanostructures. To explore morphology/size-oriented delivery performance optimization, here, we synthesized three novel cylindrical polymer brushes (CPBs) by atom transfer radical polymerization (ATRP), which were cellulose-*g*-(CPT-*b*-OEGMA) (CCO) with different lengths (~86, ~40, and ~21 nm). The CPBs are composed of bio-degradable cellulose as the carrier, poly(ethylene glycol) methyl ether methacrylate (OEGMA) as hydrophily block, and glutathione (GSH)-responsive hydrophobic camptothecin (CPT) monomer as loaded anticancer drug. By controlling the chain length of the initiator, three kinds of polymeric prodrugs with different lengths (CCO-1, CCO-2, and CCO-3) could be self-organized into unimolecular micelles in water. We carried out comparative studies of three polymers, whose results verified that the shorter CPBs exhibited higher drug release efficiency, more cellular uptake, and enhanced tumor permeability, accompanied by shortened blood circulation time and lower tumor accumulation. As evidenced by *in vivo* experiments, the shorter CPBs exhibited higher anti-tumor efficiency, revealing that the size advantage has a higher priority than the anisotropic structure advantage. This provided vital information as to design an anisotropic polymer-based drug delivery system for cancer therapy.

1. Introduction

Over the past few decades, nanostructures with well-defined size and morphology have been prepared by the self-organized of amphiphilic block copolymers which have been extensively explored in many fields, not only for the aesthetics but also for their wide applications in nanomedicine, sensors, microreactor, catalysis and biomimicry [1–3]. The dendritic-form [4], comb-form [5] and star-like [6] polymers integrated with hydrophilic and hydrophobic parts have exhibited exciting activity on the biological application. Depending on their chemical structure, amphiphilic polymers can self-organize into various morphologies, such as fibers, vesicles, worm-like or spherical micelles [7]. Additionally, the

size and morphology of the self-organized micelles can be further adjusted with several factors, such as the hydrophilic-hydrophobic ratio, carrier morphology, and grafting rate [8,9]. It was worth noting that the size and morphology played critical roles in drug dynamic *in vivo* behavior, in particular their pharmacokinetics and biodistribution [10–13]. Nevertheless, there has been still lacked investigations on the comparisons of therapeutic effect resulted from varied particle size and morphology in a single system until now. (see Scheme 1)

Natural polysaccharide has been widely applied in polymer-carriers attributing to their poly-hydroxyl, facile chemical modification, good biocompatibility, and degradability, including cyclodextrin [13], dextran [14], konjac [15], cellulose [16], and etc. By chemical

modification of backbone with hydrophilic and hydrophobic copolymer block, the obtained amphipathic copolymer can be self-organized into unimolecular micelles in water [17,18]. As one type of unimolecular micelles, cylindrical polymer brushes (CPBs), also known as "molecular bottlebrushes", were a class of polymers with anisotropic structure, have shown superior morphological and biological advantages compared with isotropic materials in the field of nanomedicine, including a special rod-like structure, easily and accurately controllable draw ratio, high drug loading rate, controllable hydrophilic/hydrophobic ratio and stability [19,20]. However, few investigations have been performed on the detailed *in vitro* and *in vivo* characterization of anisotropic CPBs. Thus, it is desperately needed to design, synthesize, and characterization of a series of innovative amphiphilic CPBs with varying lengths, as well as the self-organized unimolecular micelles.

Herein, the well-designed amphiphilic polymers of cellulose-*g*-(CPT-*b*-OEGMA) (CCO) were firstly prepared, integrating the hydrophobic part of reduction-responsive camptothecin (CPT) monomer and the hydrophilic part of an oligomer poly (ethylene glycol) methyl ether methacrylate (OEGMA). By controlling the length of the cellulose backbone, the obtained polymers could be self-organized into the CPBs with different length (~86 nm in CCO-1, ~40 nm in CCO-1, and ~21 nm in CCO-3). Both *in vivo* and *in vitro* investigations demonstrated that the CPB-based drug delivery system showed unique advantages for enhancing the effectiveness of chemotherapy.
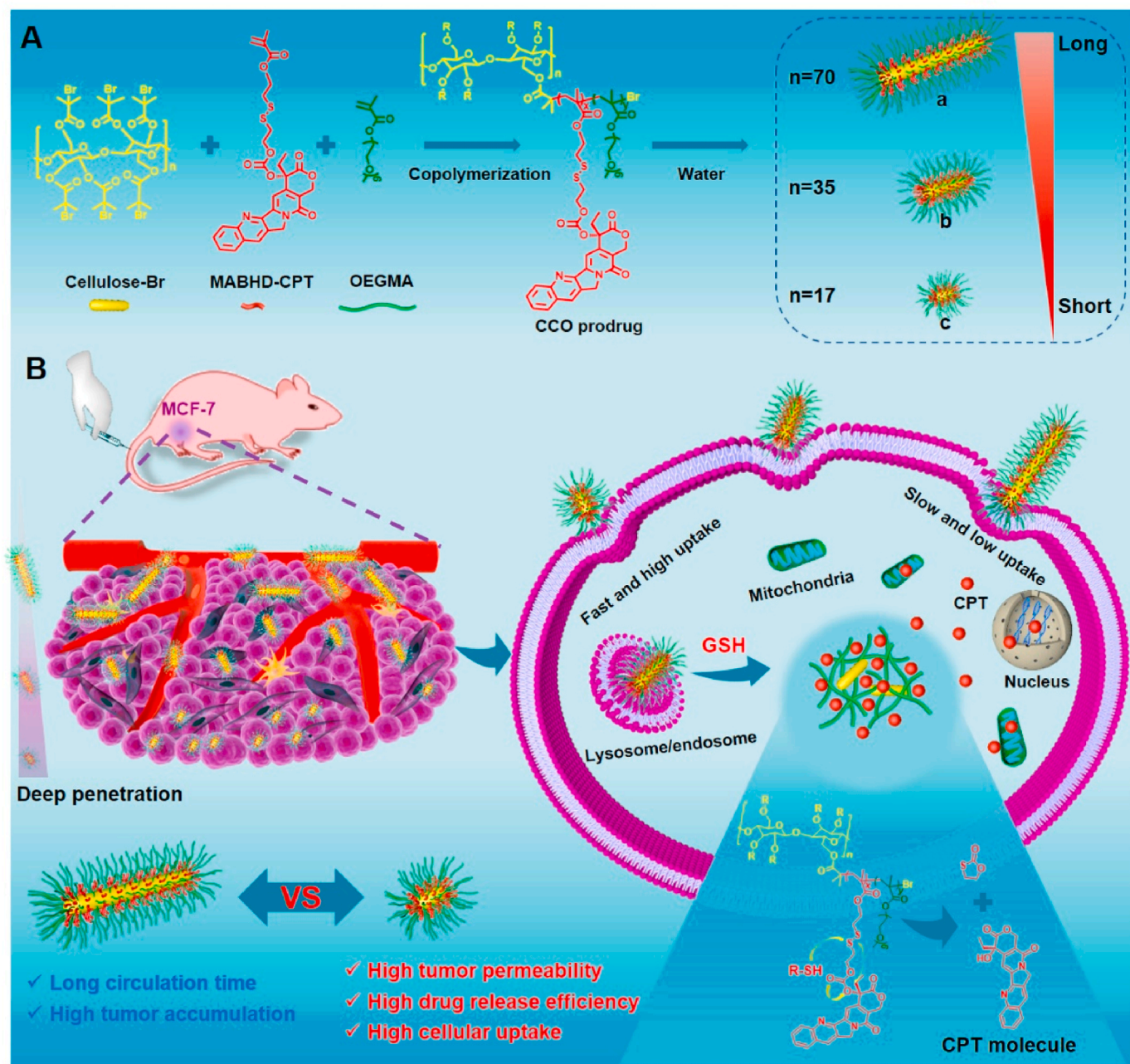
Scheme 1. Schematic representation of the synthesis and functional pattern of CCO micelles for enhancing the effectiveness of chemotherapy. (A) Synthetic route of CCO prodrug and self-organize into micelles with three different lengths in water (top panel). (B) Schematic diagram of tissue infiltration and cell internalization. CPBs with longer length showed a prolonged blood circulation time and preferable tumor accumulation, while shorter ones showed enhanced tumor permeability, higher drug release efficiency, and cellular uptake rate.

2. Experimental section

2.1. Materials

The 6-hydroxyhexyl methacrylate (MABHD) modified camptothecin (SCPT) [14,21] and 1-allyl-3-methylimidazolium chloride [22] were synthesized according to previously reported literatures. All chemical reagents were commercially available and used as received unless otherwise noted. CPT was obtained from Adamas-beta® (China). Cellulose (microcrystalline), 2-bromoisobutyrylbromide (BiBB), allyl chloride, 1-methylimidazole, oligomer poly (ethylene glycol) methyl ether methacrylate (OEGMA), Copper (I) bromide (CuBr), tri[2-(dimethylamino) ethyl]amine (Me$_6$TREN), triphosgene (BTC), 2-hydroxyethyl disulfide (BHD), Nile Red, N, N-dimethylformamide (DMF), dimethyl sulfoxide (DMSO), triethylamine (TEA) and 1-methyl-2-pyrrolidone (NMP) were obtained from Sigma-Aldrich (USA).

All consumable items used for cell assay, such as Dulbecco's Modified Eagle's Medium (DMEM), phosphate buffered saline (1 × PBS, PH = 7.4), TrypLE™ Express Enzyme (1 ×), fetal bovine serum (FBS), penicillin/streptomycin liquid (PS), 3-(4,5-dimethylthiazol-2-yl)-2,5-diphenyltetrazolium bromide (MTT), Alexa Fluor® 488 phalloidin (AF-488), Lyso-Tracker Red, Mito-Tracker Green, live/dead viability kit and 1,1′-dioctadecyl-3,3,3′,3′-tetramethylindotricarbocyanine iodide (Dir) were purchased from Life Technologies (China). terminal deoxynucleotidyl transferase-mediated dUTP-biotin nick end labeling (TUNEL) apoptosis assay kit were purchased from Beyotime Biotechnology (China).

2.2. Synthesis of cellulose-Br macroinitiators

Preparation of macroinitiators was completed in two steps. In the first step, 5.0 g of cellulose was dried in a vacuum oven at 80 °C overnight, and then the water in cellulose was removed by co-boiling with anhydrous toluene. The macroinitiator of cellulose-Br was synthesized according to previously reported literature [16]. 5.0 g of cellulose was dissolved in 50 g of 1-allyl-3-methylimidazolium chloride, and 20 mL of DMF and 20 mL of NMP was added to the solution. Then excessive 2-bromoisobutyrylbromide (BIBB) was gradually injected into the solution at 0 °C and reacted in the dark overnight. The product mixture was purified by precipitating 3 times in water, and a white powder of cellulose-Br intermediate was obtained.

In the second step, 5.0 g of cellulose-Br intermediate was dissolved in 40 mL of NMP, and then 10 mL of BiBB was added for a second modification to obtain the highest density of reactive sites. Afterward, a fraction precipitation method was applied to obtain 9 kinds of cellulose-Br product with different narrow molecular weight dispersion. Three of them were selected for further researches, which were named cellulose-Br-1, cellulose-Br-2, and cellulose-Br-3, respectively.

2.3. Synthesis of cellulose-g-(MABHD-SCPT-b-OEGMA) (CCO) polymers

The amphiphilic polymer was synthesized by one-step copolymerization with the cellulose-Br as a macroinitiator: cellulose-Br (cellulose-Br-1, cellulose-Br-2 or cellulose-Br-3, 18.18 mg, equivalent to 0.09 mmol -Br), SCPT (161 mg, 0.027 mmol), OEGMA (450 mg, 0.9 mmol), Me$_6$TREN and CuBr (12.91 mg, 0.09 mmol) were dissolved with DMSO in a glovebox. The reaction then occurred in dark at 25 °C overnight and the final product was purified by dialyzing against THF. The product of CCO-1, CCO-2, and CCO-3 was obtained.

2.4. Preparation of prodrug micelles

Briefly, 10 mg of CCO was dissolved in 1 mL of THF and then dispersed into 8 mL of DI water under stirring. The solution was then dialyzed against DI water (MWCO = 3.5 kDa) for 2 days to remove the organic solvent. Then, the obtained CCO micelles were applied for the following assays.

2.5. In vitro release of CCO

Firstly, CCO micelles were dispersed in PBS (DTT = 50 mM) to 50 μg mL^{-1}, and the solution was shaken at 37 °C for 24 h. The drug loading rate of CPT was calculated according to a standard curve of the fluorescence intensity corresponding to a known concentration. (Excitation wavelength: 365 nm; Emission wavelength: 430 nm). The release assay was performed at 37 °C for 24 h, under a horizontal shaking at 130 rpm. Specifically, 1.0 mL of CCO micelles (500 μg mL^{-1}) in a dialysis bag (MWCO = 3.0 kDa) was immersed in 80 mL of PBS (pH = 7.4) containing 0, 2 μM or 10 mM DTT (reagent that mimics GSH *in vitro*). Then, 1 mL of release medium was sampled at certain time points and then an equivalent volume of fresh PBS was added to the solution. The concentration of CPT was determined by fluorescence spectroscopy.

2.6. Cell culture

Human cervical cancer cell line (HeLa), human breast cancer cell line (Michigan Cancer Foundation-7, MCF-7), and mouse fibroblasts cell line (L929) were all originally obtained from the cell bank of American Type Culture Collection (ATCC). The cells were cultured in DMEM supplemented with 10% FBS and 1% PS at 37 °C in a humidified environment with 5% CO$_2$.

2.7. Cytotoxicity assay

HeLa, MCF-7, and L929 cells were treated with free CPT or CCO micelles and then the cell viability was tested by MTT assays. Briefly, cells were seeded in a 96-well culture plate with a density of 10^4 cells per well. After cell adhesion, the culture medium was replaced with a fresh medium containing a certain concentration of free CPT and CCO micelles. After the cells were treated for 72 h, the medium was removed and followed by adding 200 μL of MTT solution (0.5 mg mL^{-1}) in each well. After incubating for another 4 h, the formazan was dissolved with 100 μL of DMSO, the absorbance of each well was measured by a microplate reader at 570 nm (Tecan SPARK-10 M plate reader).

2.8. Live/dead staining

The toxicity of micelles on tumor cells was further evaluated with a live/dead staining test. MCF-7 cells were seeded in a 12-well culture plate, with a density of 1.5×10^5 cells per well. After cell adhesion, the culture medium was replaced with a fresh medium containing 10 μg CPT/mL of CCO. After incubating for another 24 h, the cells were stained with a live/dead staining kit for 20 min and observed with a fluorescence microscope (Olympus IX71).

2.9. Apoptosis analysis

HeLa cells were seeded in 12-well plates, with a density of 10^6 cells per well. The cells were cultured for 12 h and followed by adding fresh culture medium containing 20 μg CPT/mL of CCO, the cells without treatment were applied as a control. After incubating for another 24 h, the floating and attached cells were collected, then stained with Annexin V-FITC and propidium iodide (PI). Finally, the cells were analyzed with flow cytometry (FCM, NovoCyte 2060R, USA).

2.10. Cellular uptake

HeLa cells were seeded in 12-well plates with a density of 10^6 cells per well and then cultured overnight. After cell adhesion, the fresh culture medium containing 20 μg CPT/mL of Nile red (NR)-loaded CCO micelles were added. The cells were treated for 10 min, 30 min, 1 h, 2 h, 4 h, and then washed with PBS. The cellular uptake was detected with

flow cytometry.

2.11. CLSM imaging

HeLa cells were seeded in 8-well plates with a density of 3×10^4 cells per well, and then treated with CCO containing 20 μg mL^{-1} of CPT for 2 h or 6 h. After then, the cells were fixed with formalhyde for 30 min, followed by staining with AF-488 and DRAQ5. Finally, the cells were washed with PBS 3 times and observed by confocal laser scanning microscopy (CLSM, Carl Zeiss 800, Germany). Similarly, HeLa cells treated with CCO micelles containing 20 μg mL^{-1} of CPT were also stained with Lyso-Tracker Red or Mito-Tracker Green for 40 min. The images were taken by CLSM.

2.12. Tumor penetration in vitro and in vivo

The tumor penetration behaviors of the CCO micelles *in vitro* were investigated with MCF-7 induced multicellular spheroid (MCSs) tumor model. Briefly, 50 μL of 1% agarose was pre-added into a 96-well plate, then MCF-7 cells were seeded into the well with a density of 1.0×10^3 cells per well. The tumor spheroids were formed after the cells were incubated for 5–7 days. The medium was removed and 200 μL of fresh medium containing CCO micelles (with CPT concentration of 20 μg mL^{-1}) were added. The MCSs were incubated for 8 h, and the penetrating ability was examined by CLSM.

2.13. Animals and xenograft tumor models

BALB/c nude mice (4–5 weeks, 18–20 g, female) applied in biodistribution and therapeutic effectiveness evaluation and Kunming mice (KM, 4–5 weeks, 20–25 g, female) applied in routine blood test were supplied by Dashuo Experimental Animal Co. Ltd. (Chengdu, China) and Tengxin Biological Technology Co. Ltd. (Chongqing, China), respectively. All animal assays were performed according to the animal study guidelines approved by the University Committee on Use and Care of Animals (UCUCA) at Southwest University. 4×10^6 MCF-7 cells were suspended in 125 μL of culture medium and subcutaneously injected into the right armpit of female nude mice to establish the xenograft tumors. The tumor size was measured every day and when the tumor volume reached about 100 mm^3, the mice were randomly divided into four groups (n = 6).

2.14. Hemolysis experiment

The murine blood was collected and centrifuged at 5.0×10^3 rpm for 5 min. The erythrocytes in the precipitate pellet were washed with PBS for several times until no color could be observed in the supernatant. CCO CPBs were added in and obtaining an ultimate CPT concentration of 1, 5, 25, 125 or 250 μg mL^{-1}. The samples were incubated at 37 °C in a shaking container for 1 h. After centrifuging at 3000 rpm for 5 min, the supernatant was tested by a microplate reader at 575 nm. The erythrocytes incubated with PBS or 1% TritonX-100 were served as the negative control and positive control, respectively. The percentage of hemolysis was calculated as follows:

Hemolysis % = [(Sample absorbance – Negative control)/(Positive control – Negative control)] × 100%.

2.15. In vivo biodistribution

MCF-7 tumor-bearing nude mice were injected with free Dir and CCO@Dir with a Dir dose of 150 μg mL^{-1}. After 24 h, the mice were sacrificed and the major organs were collected, including heart, liver, spleen, lung, kidney, and tumor. The images were taken by Near-Infrared Ray (NIR) imaging system (PerkinElmer IVIS Lumina Kinetic Series III). On this foundation, the tumor penetration *in vivo* was also evaluated. MCF-7 tumor-bearing nude mice were pre-injected with CCO

micelles for 24 h. The tumors were collected and cut into slices, and the slices were directly observed by CLSM.

2.16. Pharmacokinetics in vivo

Free CPT or CCO micelles were injected into SD rats with CPT concentration equivalent to 5 mg kg^{-1}. Then blood was collected from the orbital venous plexus at 10 min, 20 min, 30 min, 1 h, 2 h, 3 h, 5 h, 7 h, 12 h or 24 h post-injection. The blood samples were centrifuged at 10,000 rpm for 10 min, and 15 μL of DTT (0.1 N) were added in 15 μL of plasma to cleave the CPT. 30 μL of HCl (0.1 M) was added during ice bath and followed by adding 200 μL of methanol. The blood samples were then incubated for 4 h at 4 °C for protein removal. After centrifuging for 10 min at 14000 rpm, the supernatant was detected with a microplate reader.

2.17. Routine blood test

Routine blood tests and biochemical index analyses were carried out to assess the potential toxicology of the CCO micelles. Kunming mice were injected with normal saline and CCO micelles through the tail vein. After 1 day or 7 days, the blood was collected from the eye socket for routine blood examination (n = 4). The routine blood test involved parameters including white blood cell count (WBC), lymphocyte ratio (LYM), red blood cell count (RBC), hemoglobin concentration (HGB), hematocrit (HCT), mean corpuscular hemoglobin concentration (MCHC), variation coefficient of red blood cell distribution width (RDW), platelets (PTL) and mean platelet volume (MPV) index. The routine blood test was carried out by a hematology analyzer (Mindray BC-2600Vet).

2.18. In vivo anti-tumor efficacy evaluation

To investigate the anti-tumor efficacy of CCO micelles, MCF-7 tumor bearing nude mice were randomly grouped (n = 6) when tumors volume reached about 100 mm^3. The mice were treated with normal saline, CCO-1, CCO-2, or CCO-3 through the tail vein, with CPT concentration equivalent to 5 mg kg^{-1}. The treatment was repeated for a total of four times, on day 1, 4, 7, and 10. During the treatment, the tumor size and body weight were monitored every 2 days. Tumor volumes were calculated with the following formula: V = 1/2 × (Tumor Length) × (Tumor Width)^2.

2.19. Tissue histological evaluation

The tumor, heart, liver, spleen, lung, and kidney tissues were collected and fixed with 4% paraformaldehyde for 24 h. The samples were embedded in paraffin and cut into slices. The fixed slices were stained with hematoxylin and eosin (H&E) or terminal deoxynucleotidyl transferase-mediated dUTP-biotin nick end labeling (TUNEL) for exploring the tissue toxicity or apoptosis of tumor cells.

3. Results and discussion

The 1-allyl-3-methylimidazolium chloride ([AMIM]Cl) was synthesized according to the previous report [23], and the chemical structure of [AMIM]Cl was verified by ^{1}H NMR (Bruker AVANCE 600 MHz NMR, Figure S1-S2). The CPT monomer (SCPT) was synthesized by silica gel column chromatography with three steps, achieving a high yield (>60%) and purity (Figure S3-S6). The cellulose initiator cellulose-Br was also successfully synthesized and fully characterized by ^{1}H NMR, FT-IR (Thermo Nicolet 6700), and gel permeation chromatography (GPC, Agilent 1206) (Figures S7-S10). The amphiphilic polymers CCO-1, CCO-2, and CCO-3 were synthesized through the copolymerization of hydrophobic SCPT and hydrophilic OEGMA by ATRP. The final product was confirmed by ^{1}H NMR and FT-IR (Figure S11-S12, Fig. 1E). These
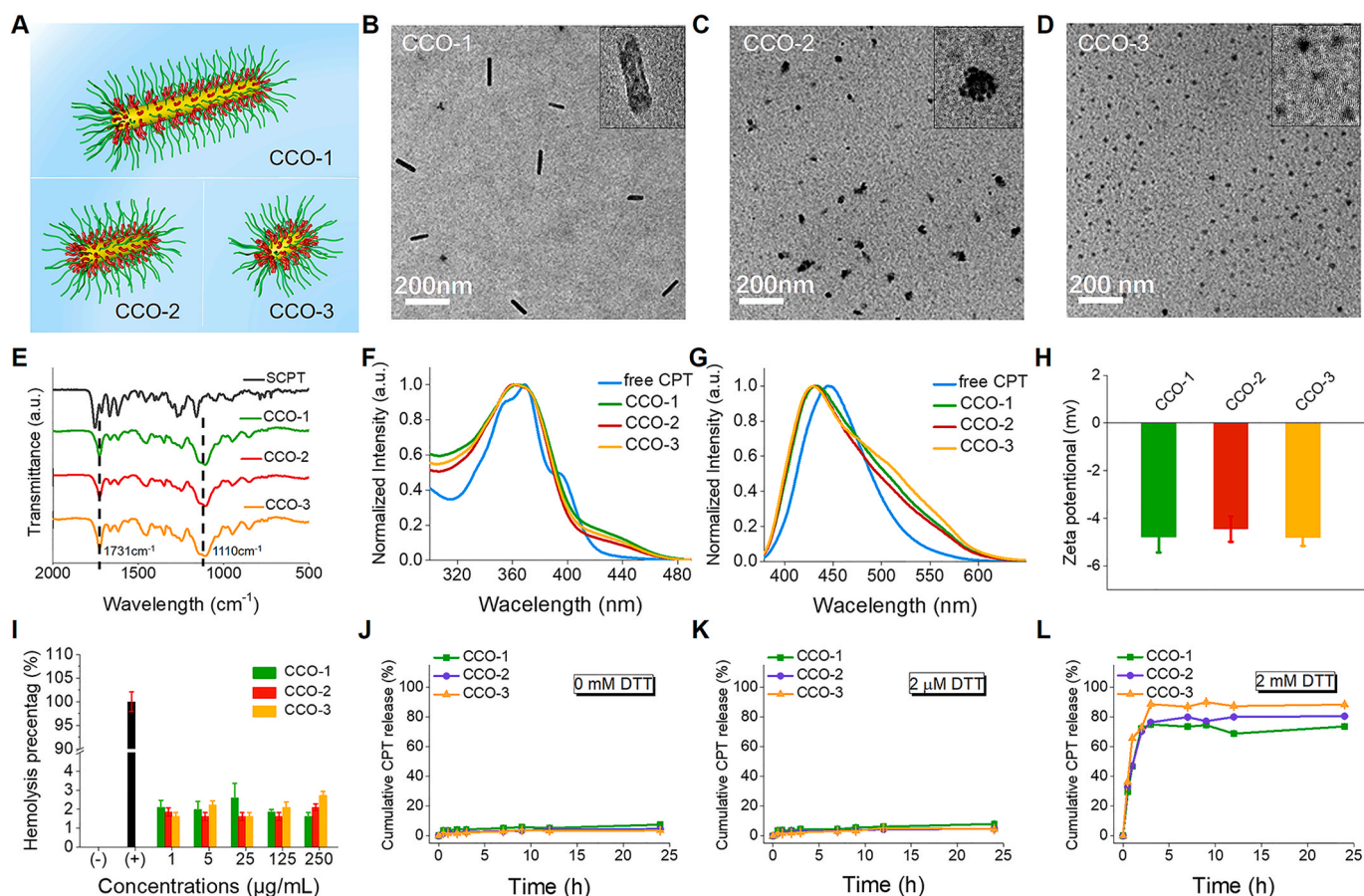
Fig. 1. Characterization of CCO micelles. (A) Diagrammatic representation of CCO-1, CCO-2, and CCO-3 micelles. TEM images of (B) CCO-1, (C) CCO-2, (D) CCO-3. (E) FT-IR spectra of CPT monomer, CCO-1, CCO-2, and CCO-3. (F) UV–vis spectra and (G) fluorescence spectra of free CPT, CCO-1, CCO-2, and CCO-3. (H) Zeta potential and (I) hemolysis of CCO-1, CCO-2, and CCO-3. CPT release behavior triggered with DTT of (J) 0 mM, (K) 2 μM, and (L) 2 mM.

results suggested that SCPT and OEGMA were successfully introduced into the cellulose backbone. Next, the prodrug CCO-1, CCO-2 and CCO-3 were self-organized into unimolecular micelles in water. The fluorescence (FL, Shimadzu RF-5301PC) and ultraviolet (UV, Shimadzu UV-1800) spectra of CCO micelles were investigated to further illustrate the successful load of CPT (Fig. 1F and G). The micelles have shown strong absorbance bands at 365 nm in UV-spectrum and maximum emission at 430 nm, indicating the successful polymerization of CPT. Previous studies showed that the micellar morphologies could be controlled by tuning the aspect ratio (backbone length and graft ratio) of block copolymers [8,16]. As we expected, the CCO polymers were self-organized into different morphologies, which was associated with the initiators of different lengths. As shown in Fig. 1A, polymers prepared by cellulose-Br with high molecular weight tend to form micelles with long-rod structure, while cellulose-Br with low molecular weight would form micelles with short-rod structure. The transmission electron microscope (TEM, JEM-1230EX) images of CCO-1, CCO-2, and CCO-3 suggested a mean length of 86 ± 15 nm (diameter: 16 ± 3 nm), 40 ± 9 nm, and 21 ± 4 nm, respectively (Table S1 and Fig. 1B–D). The CCO-1, CCO-2, and CCO-3 micelles showed a slightly negative surface charge of −4.8, −4.5, and −4.8 mV, respectively. It was benefited to prolong blood circulation time [24–26] (Fig. 1H). Furthermore, the prodrug bio-safety was also investigated by hemolysis experiment. The results indicated that no obvious hemolysis was observed even in a high concentration of 250 μg mL^{-1} (Fig. 1I).

The reductive tumor microenvironment has been a widely applied intracellular stimulator for achieving the selective release of therapeutic agents [23,27,28]. The GSH concentration in tumor cells (2–10 mM) was much higher than normal cells (2 μM) [29,30]. The GSH-sensitive

micelles could maintain stability in normal tissues and during blood circulation, while disassembled in the tumor microenvironment to release the drug from carriers. DTT was a prevalent GSH simulant, which was applied to investigate the loading rate and release behavior of CCO micelles. Firstly, the loading rate of micelles was conducted by incubating 1 mL of micelles with 50 mM of DTT for 24 h. The loading capacities of CCO-1, CCO-2, and CCO-3 were measured to be 16.2 wt%, 24.1 wt%, and 26.2 wt%, respectively. Then, the *in vitro* reduction-responsive drug release behavior of CCO micelles were investigated. As shown in Fig. 1J–L, the CPT was gradually released from the carriers with increased incubation time in 2 mM DTT. The cumulative CPT release of CCO-1, CCO-2 and CCO-3 was over 73.6%, 80.6%, and 88.3%, respectively. CCO-3 showed higher cumulative release because of its smaller size, which caused a faster and more easily complete degradation. On the contrary, all three micelles incubated in 2 μM or 0 μM DTT showed no significant drug release, which further proved the tumor-specific drug release behavior of this drug delivery system.

It was noteworthy that selective killing of tumor cells while harmless to normal cells was the premise and foundation of cancer therapy. The selective toxicity of CCO micelles to tumor cells was also investigated in this study, which was directly associated with the therapy efficiency. A series of experiments were applied to evaluate the therapy efficiency of polymer micelles, including MTT, live/dead, and cell apoptosis assay. For MTT assay, HeLa, and MCF-7 were applied as representative tumor cells, and L929 as normal control. As shown in Fig. 2A–C, after incubation with CCO micelles for 72 h, HeLa and MCF-7 cells were significantly killed, while little damage was observed on L929 cells. Obviously, CCO-3 presented prominent cytotoxicity, with the tumor cell viability as low as 10%. It may be on account of its smaller size. Notably, the cell
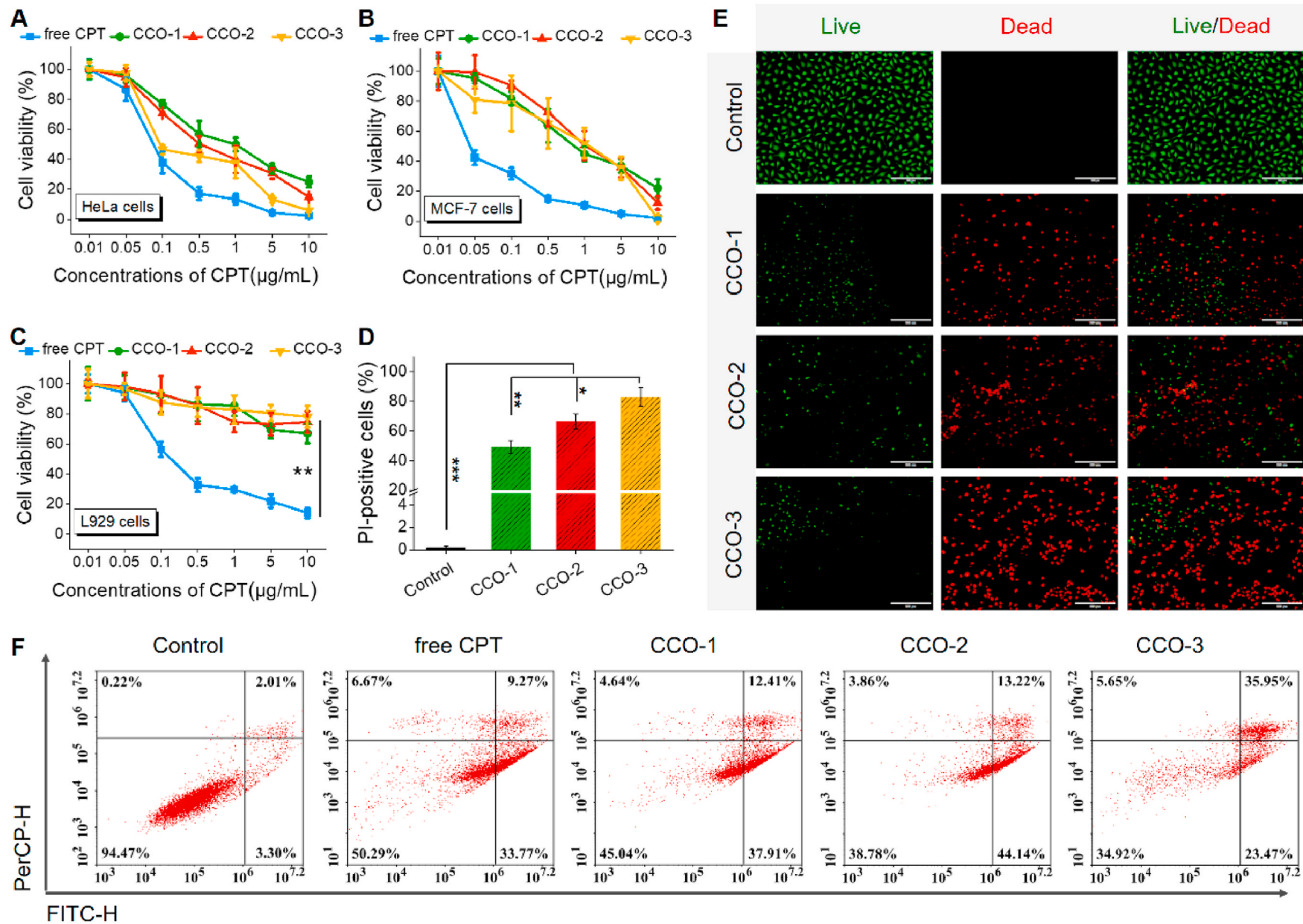
Fig. 2. The selective cell apoptosis induced by CCO micelles. Cell-viability assay in tumor cells of (A) HeLa, (B) MCF-7, and normal cells of (C) L929 incubated with free CPT, CCO-1, CCO-2, and CCO-3 micelles. (D, E) Live/dead assay and the corresponding percentage of PI-positive cells in MCF-7 cells incubated with CCO micelles. The scale bar was 200 μm. (F) Cell apoptosis of free CPT, CCO-1, CCO-2, and CCO-3 micelles.

viability of L929 cells remained up to 65% when the CPT concentration reached 10 μg mL^{-1}. However, the free CPT showed strong toxicity to both tumor cells and normal cells. The live/dead assay was conducted for a more intuitive view of the proportions for both live and dead cells. As shown in Fig. 2D and E, the result was in accord with the MTT assay. Compared with free CPT, cells treated with CCO micelles showed strong toxicity, shown as strong red fluorescence, and similarly, CCO-3 presented higher cytotoxicity. Further, FCM was applied for verifying the cytotoxicity of CCO micelles by cell apoptosis assay. The same tendency was observed in the FCM-based cell apoptosis assay (Fig. 2F). The percentage of apoptotic HeLa cells was 43.0%, 50.3%, 57.4%, and 59.4% after the treatment of free CPT, CCO-1, CCO-2, CCO-3 micelles, respectively. Based on the above results, it can be observed that, compared to other micelles, the CCO-3 micelles with the smaller size can be internalized effectively, resulting in higher drug utilization. Thus, higher efficacy to induce tumor cell apoptosis can be realized.

Furthermore, the distributions and cellular uptake behaviors of CCO micelles were investigated by CLSM and FCM. For CLSM, the skeleton and nucleus of HeLa cells were stained with AF-488 and DRAQ5, and emitted green and red fluorescence, respectively. As observed in Fig. 3A, the merged images showed that the drug was uniformly released within the cell, indicating that CPT was released successfully. In addition, the cellular uptake behavior of the micelles was also quantitatively determined by FCM. As shown in Fig. 3D–E, it was found that HeLa cells treated with CCO-3 showed the maximum uptake rate, compared to that of all other groups, revealing a particle size-mediated cellular uptake behavior.

The time course of the cellular localization process was also monitored by CLSM. HeLa cells were stained with a lysosome marker (Lyso-Tracker Red). The colocalization of CPT (blue fluorescence) and lysosome (red fluorescence) exhibited as magenta fluorescence in the merged images (Fig. 3B). It showed that the fluorescence of micelles and lysosomes were colocalized perfectly after incubating for 2 h, suggesting the endolysosomal pathway. To confirm whether the released CPT could enter mitochondria, HeLa cells were stained by Mito-Tracker Green, and the colocalization of CPT (blue fluorescence) and mitochondria (green fluorescence) exhibited as cyan fluorescence in the merged images. As shown in Fig. 3C, the results indicated that the drug successfully entered mitochondria. These data demonstrated a clear pathway of drugs entered the tumor cells, in which micelles would be accumulated in lysosomes prior to migrating to mitochondria.

Micelles with different size and morphology had varied performance in tumor tissue penetration [31–33]. Previous studies have demonstrated that micelles with smaller size showed enhanced *in vivo* performance through deeper penetration ability in solid tumors. In addition, rod-like micelles exhibited enhanced tumor penetration ability in comparison with spherical micelles under the same dimension [34–36]. The specificity of CCO micelles in morphology and size motivated us to investigate its potential for drug delivery. The schematic diagram of the penetration depth of CCO micelles was presented (Fig. 4A). In our study, MCSs derived from MCF-7 cells were utilized as *in vitro* model to explore the penetration ability of CCO micelles. MCSs were a widely applied three-dimensional (3D) solid tumor simulation system because its morphology and pathophysiological conditions were similar to real tumor tissues, which were proved to have more advantages over two-dimensional (2D) tumor simulation systems in cancer researches [37,38]. As shown in Fig. 4B, MCSs were incubated with different drug formulations (containing 20 μg mL^{-1} of CPT) for 8 h and then observed with CLSM Z-stack scanning. After the treatment of CCO, it was observed that the CPT with blue fluorescence was uniformly distributed on MCSs. At the scanning depth of 70 μm, the CPT fluorescence was mostly located on the edge of MCSs for the CCO-1 treated group. However, the blue
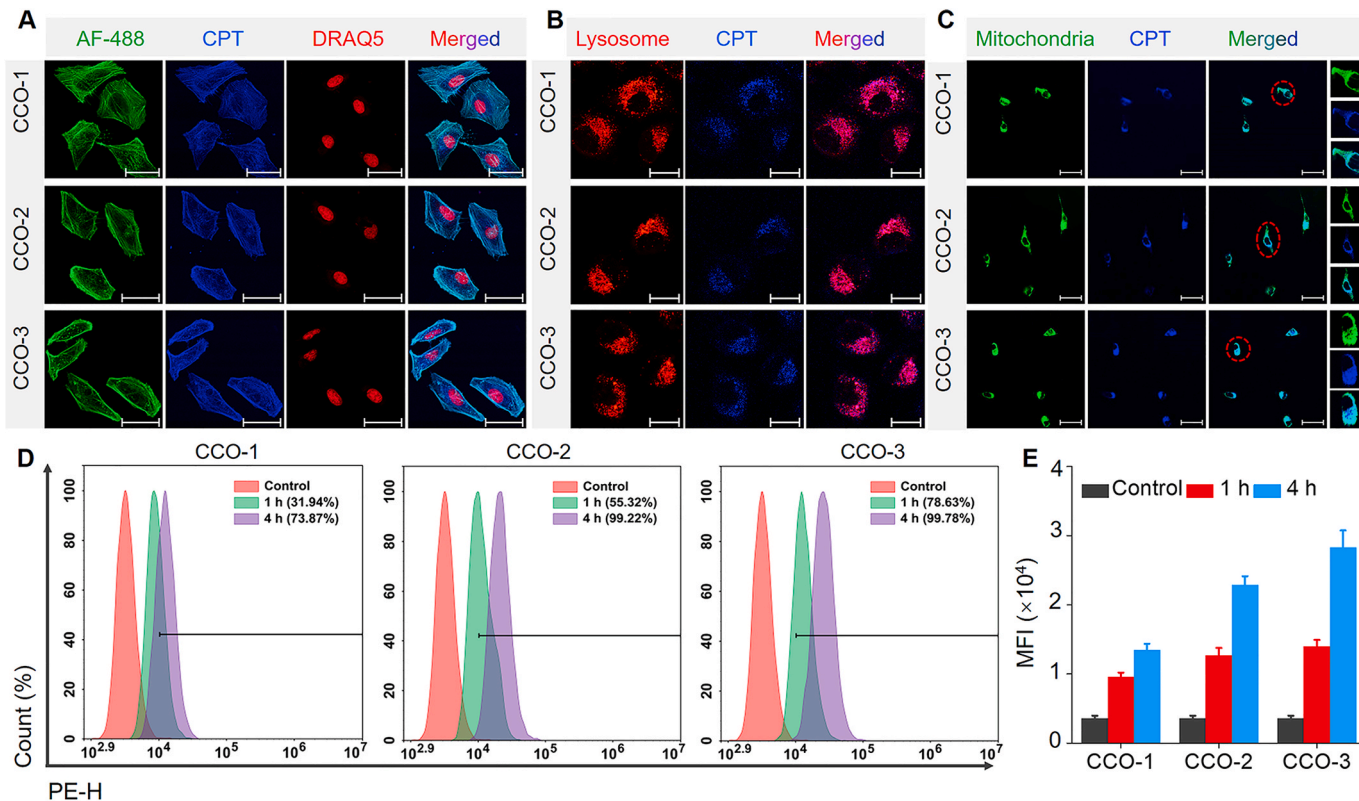

Fig. 3. Intracellular distribution and cellular uptake analysis. CLSM images of the (A) cellular uptake, (B) lysosomal and, (C) mitochondrial colocalization of CCO-1, CCO-2, and CCO-3. The scale bar was 50 μm. The right panel were the ~2-fold enlarged images of mitochondrial colocalization. (D) FCM analysis of the cellular uptake of NR-loaded CCO-1, NR-loaded CCO-2, and NR-loaded CCO-3. (E) Mean fluorescence intensity of NR-loaded CCO micelles. Data were expressed as means ± SD (n = 3).
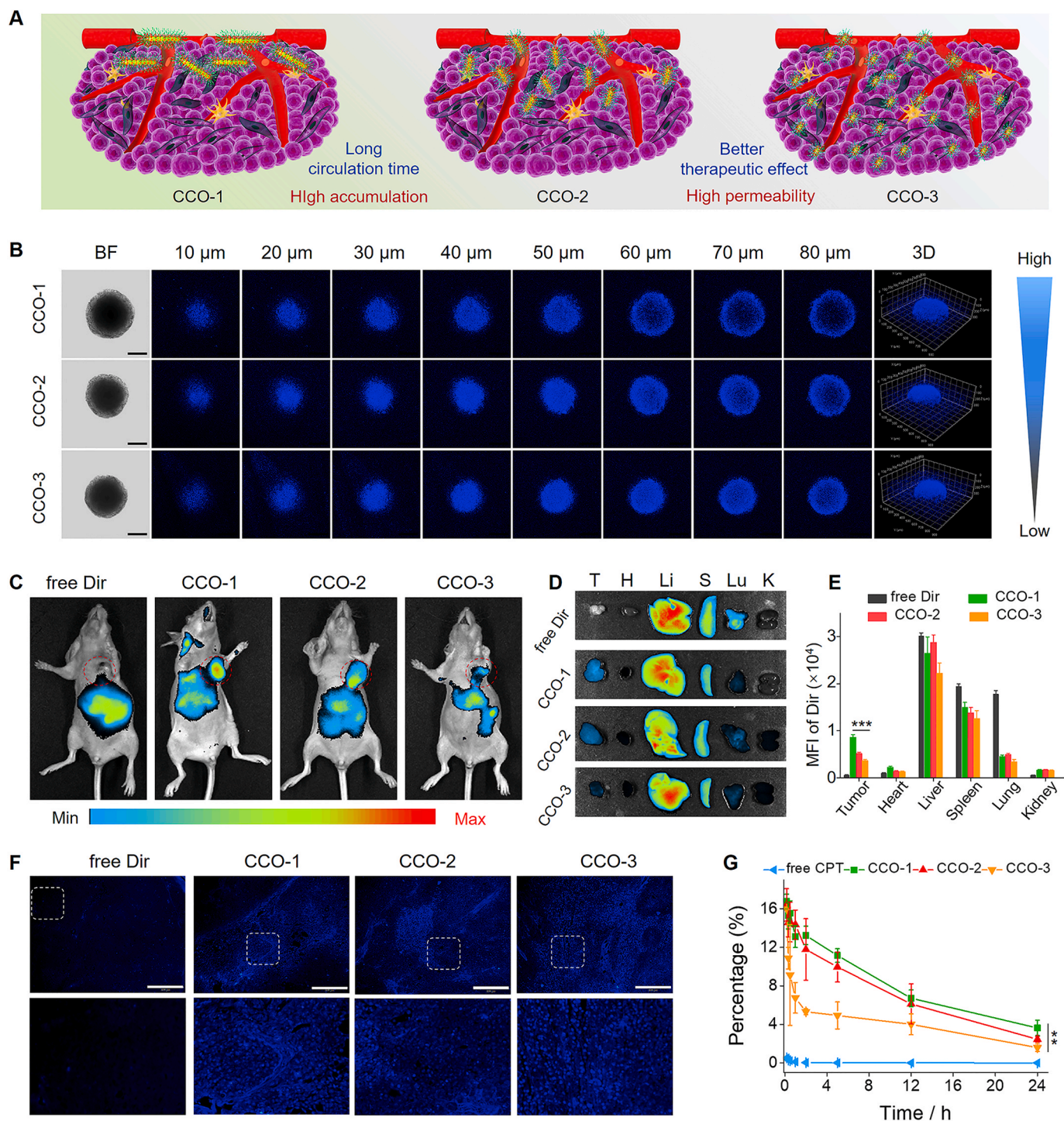
Fig. 4. Biodistribution and pharmacokinetic profiles of CCO micelles *in vivo* and *ex vivo*. (A) Schematic representation of tissue permeability of CCO-1, CCO-2, and CCO-3 micelles. (B) CLSM images of tumor penetration of CCO-1, CCO-2, and CCO-3 in MCF-7. The scale bar was 200 μm. (C) Biodistribution of free Dir and CCO micelles *in vivo*. (D) *Ex vivo* fluorescence imaging of the distribution of free Dir and CCO micelles in tumor and main organs. Mean fluorescence intensity of Dir in the tumor and main organs 24 h after injection. (F) Distribution of CPT in tumor tissues at 24 h post-injection. The scale bar was 200 μm. (G) Pharmacokinetic analysis of free CPT, CCO-1, CCO-2, and CCO-3 for 24 h after injection.

fluorescence inside the MCSs was clearly observed for CCO-3 treated group, demonstrating the size effect of the CCO-3. In general, CCO-3 exhibited a superior tumor penetration capability due to its small size.

It is well known that particles with appropriate size can be preferentially accumulated in the tumor site through passive targeting, which is a process known as the enhanced permeability and retention (EPR) effect [39,40]. In this study, diverse sizes of CCO-1, CCO-2, and CCO-3

micelles promote us to explore the effect of micelles size on tumor aggregation *in vivo*. Dir was applied as the near-infrared fluorescence tracker to track the distribution of micelles in the mice. As shown in Fig. 4C, the red circles represent the tumor site of mice. In each group, Dir fluorescence was mainly distributed in the abdomen and chest, which was mainly attributed to the nonspecific uptake of CCO micelles by the reticuloendothelial system (RES). As expected, different from the

free Dir-treated group, all CCO micelles groups tended to be accumulated in tumor tissue, and the accumulation of micelles was much more than that of in adjacent muscle tissue, indicating that micelles can be passively enriched in tumor sites through the EPR effect. In addition, the CCO-1 treated group showed a higher fluorescence signal in tumor tissue than that of CCO-2 and CCO-3 after 24 h injection, resulted from its suitable size large aspect ratio, which has a longer circulation time and more likely to accumulate at the tumor site. The distribution of micelles in main organs (i.e., heart, liver, spleen, lung, and kidney) and tumor were also imaged (Fig. 4D). Consistent with *in vivo* results, the CCO-1

micelles treated group showed stronger tumor accumulation. The distribution of micelles in organs was then determined by quantifying the fluorescence intensity of Dir (Fig. 4E). Furthermore, the CPT in tumor tissue at 24 h post-injection was tested by optical imaging and the results showed that the drug could be uniformly distributed throughout the tumor (Fig. 4 F).

Long-term safety has been a significant foundation for the clinical translation of micelles. As shown in Figure S13, the main hematological parameters for the mice administrated with CCO micelles were all in normal range, including WBC (0.8–6.8×10^9 L^{-1}), LYM (55.8–90.6%),
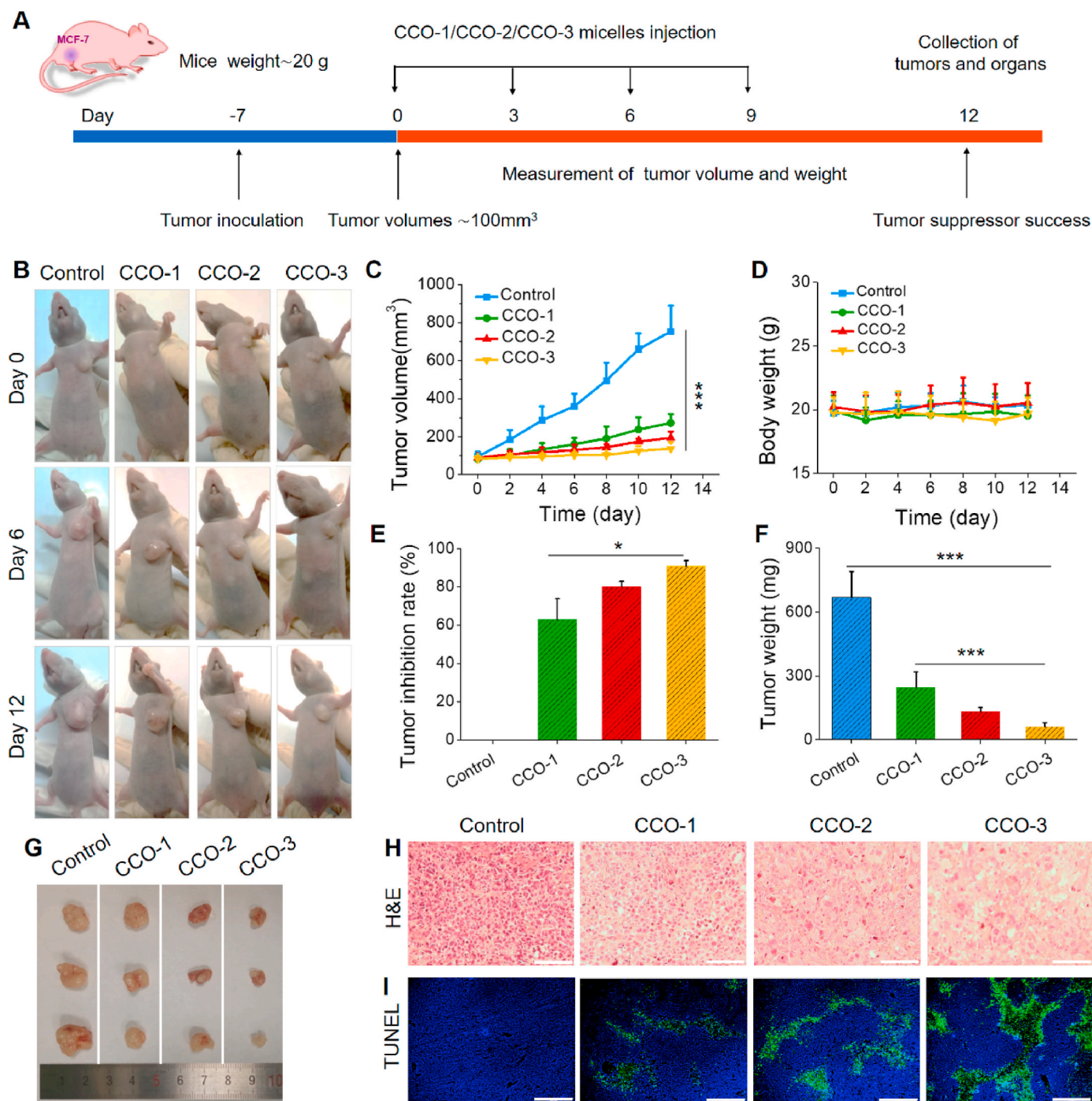

Fig. 5. *In vivo* antitumor performance of CCO micelles. (A) Schematic representation of the *in vivo* therapeutic efficacy. (B) Representative images of the mice with different treatments in 12 days. The relative variations of (C) tumor volume and (D) Body weight after the treatment of CCO-1, CCO-2, and CCO-3 micelles. (E) The tumor inhibition rate and (F) tumor weight after 12 days of treatment of CCO-1, CCO-2, and CCO-3. (G) *Ex vivo* tumor tissues after 12 days of treatment. (H) H&E and (I) TUNEL staining of tumor slices after 12 days. The scale bar was (H) 100 μm and (I) 200 μm.

RBC (6.36–9.42 × 10^{12} L^{-1}), HGB (110–143 g L^{-1}), HCT (34.6–44.6%), MCHC (302–353 g L^{-1}), RDW-SD (13.0–17.0% fL), PTL (450–1590 × 10^9 L^{-1}) and MPV (3.8–6.0 fL). The systemic toxicity of micelles was low, which was due to the fact that the micelles were stable during blood circulation with limited GSH level, which was inadequate to activate the loaded drugs.

As reported, rod-like micelles exhibited long blood circulation time than spherical [41]. To explore the pharmacokinetics of micelles, free CPT, CCO-1, CCO-2, and CCO-3 micelles were injected into the tumor-free Sprague-Dawley (SD) mice. Then the blood was sampled from the orbital venous plexus at 10 min, 20 min, 30 min, 1 h, 2 h, 3 h, 5 h, 7 h, 12 h, or 24 h post-injection. For free CPT, CCO-1, CCO-2, and CCO-3, the CPT remained in the plasma was <0.1%, 6.7%, 6.1%, and 4.0% at 12 h post-injection, respectively (Fig. 4G). Meanwhile, the area under the curve of micelles was much larger than that of free CPT, indicating that the nano-formulation can significantly prolong the blood circulation time. Moreover, the half-life of CCO-1 was relatively higher than CCO-2 and CCO-3, which was ascribed to the rod-like morphology and large size.

Furthermore, the *in vivo* anticancer activity of CCO micelles were evaluated in MCF-7 tumor-bearing nude mice. The mice were randomly divided into 4 groups (n = 5 for each group), including PBS, CCO-1, CCO-2, and CCO-3. The injection was via the tail vein at a dose of 5 mg kg^{-1} based on CPT every 3 days (Fig. 5A), and the mice were photographed before and after each treatment (Fig. 5B). Moreover, the variation of tumor size and body weight were recorded every 2 days (Fig. 5C and D). No obvious body weight variation was observed, indicating the good biosafety of the CCO-based drug delivery system. After 12 days of treatment, the tumor growth in micelles groups was suppressed to a certain extent. Comparatively, the tumor volume in the control group rapidly grew with a size increase of 8.0-fold. The tumor volume in chemotherapy groups treated with CCO-1, CCO-2, and CCO-3 was suppressed, with a size increase of 3.4, 2.2, 1.7-fold at 12 days, respectively. The CCO-3 group showed the highest inhibition rate of ∼ 90%, compared to ∼63% in the CCO-1 group and ∼80% in the CCO-2 group, which demonstrated that the size advantage was prior to anisotropic advantage (Fig. 5E). These results were also supported by the variations of average tumor weight (Fig. 5F) and tumor size (Fig. 5G) on day 12.

H&E and TUNEL staining analyses were conducted to further clarify the tumor growth inhibition mechanism of CCO micelles. At the end of treatment, these mice were sacrificed and the tumors were removed from nude mice, then sliced up and stained with H&E and TUNEL. Both H&E and TUNEL assays were applied to evaluate the pathological changes in tumor tissues. As shown in Fig. 5H–I, limited cell damage was observed in the H&E and TUNEL staining results of CCO-1 and CCO-2 groups, while the CCO-3 group exhibited much severer cell necrosis. The tissue toxicity was also observed by H&E staining of main organs, including heart, liver, spleen, lung, kidney. No significant tissue damage was observed in micelle-treated groups (Figure S14), indicating that our system could minimize the systemic toxicity.

4. Conclusions

In summary, a series of smart CCO-based CPBs have been successfully developed, involving biodegradable cellulose as the carrier, OEGMA as a hydrophilic block, and GSH-responsive hydrophobic SCPT as an anticancer drug. By virtue of initiators with three different lengths, CCO-1, CCO-2, and CCO-3 micelles were successfully prepared, and achieving regular CPBs with different lengths. Due to the differences in scale, three micelles exhibited varied cytotoxicity toward tumor cells. The differences were also reflected in cell uptake, tumor penetration ability, biodistribution, pharmacokinetics, and antitumor efficacy. Based on *in vivo* and *in vitro* results, it can be concluded that the size advantage is prior to morphology advantage. Taken together, the results in this study have provided valuable information and method for the design of intelligent drug delivery systems in chemotherapy.

CRediT authorship contribution statement

Shuang Bai: Data curation, Writing - original draft. **Die Jia:** Data curation, Writing - original draft. **Xianbin Ma:** Data curation, Writing - original draft. **Mengyun Liang:** Data curation, Writing - original draft. **Peng Xue:** Writing - original draft, Writing - review & editing. **Yuejun Kang:** Writing - original draft, Writing - review & editing. **Zhigang Xu:** Conceptualization, Writing - review & editing.

Declaration of competing interest

The authors declare no conflict of interest.

Appendix A. Supplementary data

Supplementary data to this article can be found online at https://doi.org/10.1016/j.bioactmat.2021.02.011.

References

[1] C. Cummins, R. Lundy, J.J. Walsh, V. Ponsinet, G. Fleury, M.A. Morris, Enabling future nanomanufacturing through block copolymer self-assembly: a review, Nano Today 35 (2020), 100936.

[2] Z. Ge, S. Liu, Functional block copolymer assemblies responsive to tumor and intracellular microenvironments for site-specific drug delivery and enhanced imaging performance, Chem. Soc. Rev. 42 (2013) 7289–7325.

[3] A. Rosler, G.W. Vandermeulen, H. Klok, Advanced drug delivery devices via self-assembly of amphiphilic block copolymers, Adv. Drug Deliv. Rev. 53 (2001) 95–108.

[4] P. Ge, B. Niu, Y. Wu, W. Xu, M. Li, H. Sun, H. Zhou, X. Zhang, J. Xie, Enhanced cancer therapy of celastrol *in vitro* and *in vivo* by smart dendrimers delivery with specificity and biosafety, Chem. Eng. J. 383 (2020), 123228.

[5] L. Kobylinska, I. Patereha, N. Finiuk, N. Mitina, A. Riabtseva, I. Kotsyumbas, R. Stoika, A. Zaichenko, S.G. Vari, Comb-like PEG-containing polymeric composition as low toxic drug nanocarrier, Cancer Nanotechnol 9 (2018) 11–23.

[6] C. Yang, S. Liu, S. Venkataraman, S.J. Gao, X. Ke, X.T. Chia, J.L. Hedrick, Y. Y. Yang, Structure-directing star-shaped block copolymers: supramolecular vesicles for the delivery of anticancer drugs, J. Contr. Release 208 (2015) 93–105.

[7] A. Blanazs, S.P. Armes, A.J. Ryan, Self-assembled block copolymer aggregates: from micelles to vesicles and their biological applications, Macromol, Rapid Comm 30 (2009) 267–277.

[8] M. Mullner, S.J. Dodds, T. Nguyen, D. Senyschyn, C.J.H. Porter, B.J. Boyd, F. Caruso, Size and rigidity of cylindrical polymer brushes dictate long circulating properties in vivo, ACS Nano 9 (2015) 1294–1304.

[9] Z. Zhang, L. Zhang, J. Zhao, C. Li, W. Wu, X. Jiang, Length effects of cylindrical polymer brushes on their in vitro and in vivo properties, Biomater. Sci. 7 (2019) 5124–5131.

[10] L. An, D. Zhang, L. Zhang, G. Feng, Effect of nanoparticle size on the mechanical properties of nanoparticle assemblies, Nanoscale 11 (2019) 9563–9573.

[11] D. Jia, X. Ma, Y. Lu, X. Li, S. Hou, Y. Gao, P. Xue, Y. Kang, Z. Xu, ROS-responsive cyclodextrin nanoplatform for combined photodynamic therapy and chemotherapy of cancer, Chinese Chemical Letters 32 (2021) 162–167.

[12] M. Bouchoucha, M.F. Côté, R.C. Gaudreault, M.-A. Fortin, F. Kleitz, Size-controlled functionalized mesoporous silica nanoparticles for tunable drug release and enhanced anti-tumoral activity, Chem. Mater. 28 (2016) 4243–4258.

[13] S. Bai, X. Ma, X. Shi, J. Shao, T. Zhang, Y. Wang, Y. Cheng, P. Xue, Y. Kang, Z. Xu, Smart unimolecular micelle-based polyprodrug with dual-redox stimuli response for tumor microenvironment: enhanced in vivo delivery efficiency and tumor penetration, ACS Appl. Mater. Interfaces 11 (2019) 36130–36140.

[14] S. Bai, Y.E. Gao, X. Ma, X. Shi, M. Hou, P. Xue, Y. Kang, Z. Xu, Reduction stimuli-responsive unimolecular polymeric prodrug based on amphiphilic dextran-framework for antitumor drug delivery, Carbohydr. Polym. 182 (2018) 235–244.

[15] Z. Li, Y. Su, B. Xie, X. Liu, X. Gao, D. Wang, A novel biocompatible double network hydrogel consisting of konjac glucomannan with high mechanical strength and ability to be freely shaped, J. Mater. Chem. B 3 (2015) 1769–1778.

[16] X. Pang, Y. He, J. Jung, Z. Lin, 1D nanocrystals with precisely controlled dimensions, compositions, and architectures, Science 353 (2016) 1268–1272.

[17] Y. Xiao, H. Hong, A. Javadi, J.W. Engle, W. Xu, Y. Yang, Y. Zhang, T.E. Barnhart, W. Cai, S. Gong, Multifunctional unimolecular micelles for cancer-targeted drug

delivery and positron emission tomography imaging, Biomaterials 33 (2012) 3071–3082.

[18] X. Fan, Z. Li, X.J. Loh, Recent development of unimolecular micelles as functional materials and applications, Polym. Chem. 7 (2016) 5898–5919.

[19] M. Mullner, A.H.E. Muller, Cylindrical polymer brushes-Anisotropic building blocks, unimolecular templates and particulate nanocarriers, Polymer 98 (2016) 389–401.

[20] M. Mullner, J. Yuan, S. Weiss, A. Walther, M. Fortsch, M. Drechsler, A.H.E. Muller, Water-soluble organo-silica hybrid nanotubes templated by cylindrical polymer brushes, J. Am. Chem. Soc. 132 (2010) 16587–16592.

[21] S. Bai, M. Hou, X. Shi, J. Chen, X. Ma, Y.E. Gao, Y. Wang, P. Xue, Y. Kang, Z. Xu, Reduction-active polymeric prodrug micelles based on alpha-cyclodextrin polyrotaxanes for triggered drug release and enhanced cancer therapy, Carbohydr. Polym. 193 (2018) 153–162.

[22] H. Zhang, J. Wu, J. Zhang, J. He, 1-Allyl-3-methylimidazolium chloride room temperature ionic liquid: a new and powerful nonderivatizing solvent for cellulose, Macromolecules 38 (2005) 8272–8277.

[23] K. Dutta, D. Hu, B. Zhao, A.E. Ribbe, J. Zhuang, S. Thayumanavan, Templated self-assembly of a covalent polymer network for intracellular protein delivery and traceless release, J. Am. Chem. Soc. 139 (2017) 5676–5679.

[24] X. Zhang, T. Zhang, X. Ma, Y. Wang, Y. Lu, D. Jia, X. Huang, J. Chen, Z. Xu, F. Wen, The design and synthesis of dextran-doxorubicin prodrug-based pH-sensitive drug delivery system for improving chemotherapy efficacy, Asian J. Pharm. Sci. 15 (2020) 605–616.

[25] A. Albanese, P.S. Tang, W.C.W. Chan, The effect of nanoparticle size, shape, and surface chemistry on biological systems, Annu. Rev. Biomed. Eng. 14 (2012) 1–16.

[26] T. Sun, Y.S. Zhang, B. Pang, D.C. Hyun, M. Yang, Y. Xia, Engineered nanoparticles for drug delivery in cancer therapy, Angew. Chem. Int. Ed. 53 (2014) 12320–12364.

[27] X. Guo, X. Wei, Y. Jing, S. Zhou, Size changeable nanocarriers with nuclear targeting for effectively overcoming multidrug resistance in cancer therapy, Adv. Mater. 27 (2015) 6450–6456.

[28] H. Chen, Z. Liu, B. Wei, J. Huang, X. You, J. Zhang, Z. Yuan, Z. Tang, Z. Guo, J. Wu, Redox responsive nanoparticle encapsulating black phosphorus quantum dots for cancer theranostics, Bioact. Mat. 6 (2021) 655–665.

[29] S. Mura, J. Nicolas, P. Couvreur, Stimuli-responsive nanocarriers for drug delivery, Nat. Mater. 12 (2013) 991–1003.

[30] M.H. Lee, Z. Yang, C.W. Lim, Y.H. Lee, S. Dongbang, C. Kang, J.S. Kim, Disulfide-cleavage-triggered chemosensors and their biological applications, Chem. Rev. 113 (2013) 5071–5109.

[31] W. Yu, R. Liu, Y. Zhou, H. Gao, Size-tunable strategies for a tumor targeted drug delivery system, ACS Cent. Sci. 6 (2020) 100–116.

[32] J. Ding, J. Chen, L. Gao, Z. Jiang, Y. Zhang, M. Li, Q. Xiao, S.S. Lee, X. Chen, Engineered nanomedicines with enhanced tumor penetration, Nano Today 29 (2019), 100800.

[33] X. Feng, H. Dixon, H. Glen-Ravenhill, S. Karaosmanoglu, Q. Li, L. Yan, X. Chen, Smart nanotechnologies to target tumor with deep penetration depth for efficient cancer treatment and imaging, Adv. Ther. 2 (2019), 1900093.

[34] Y. Wang, M. Zu, X. Ma, D. Jia, Y. Lu, T. Zhang, P. Xue, Y. Kang, Z. Xu, Glutathione responsive multifunctional "trojan horse" nanogel as a nanotheranostic for combined chemotherapy and photodynamic anticancer therapy, ACS Appl. Mater. Interfaces 12 (2020) 50896–50908.

[35] D. Li, Z. Tang, Y. Gao, H. Sun, S. Zhou, A bio-inspired rod-shaped nanoplatform for strongly infecting tumor cells and enhancing the delivery efficiency of anticancer drugs, Adv. Funct. Mater. 26 (2016) 66–79.

[36] X. Huang, X. Teng, D. Chen, F. Tang, J. He, The effect of the shape of mesoporous silica nanoparticles on cellular uptake and cell function, Biomaterials 31 (2010) 438–448.

[37] M. Zanoni, F. Piccinini, C. Arienti, A. Zamagni, S. Santi, R. Polico, A. Bevilacqua, A. Tesei, 3D tumor spheroid models for in vitro therapeutic screening: a systematic approach to enhance the biological relevance of data obtained, Sci. Rep. 6 (2016) 19103.

[38] B. Kwak, Y. Lee, J. Lee, S. Lee, J. Lim, Mass fabrication of uniform sized 3D tumor spheroid using high-throughput microfluidic system, J. Contr. Release 275 (2018) 201–207.

[39] J. Fang, H. Nakamura, H. Maeda, The EPR effect: unique features of tumor blood vessels for drug delivery, factors involved, and limitations and augmentation of the effect, Adv. Drug Deliv. Rev. 63 (2011) 136–151.

[40] K. Greish, Enhanced permeability and retention (EPR) effect for anticancer nanomedicine drug targeting, Methods Mol. Biol. 624 (2010) 25–37.

[41] Y. Zhao, Y. Wang, F. Ran, Y. Cui, C. Liu, Q. Zhao, Y. Gao, D. Wang, S. Wang, A comparison between sphere and rod nanoparticles regarding their in vivo biological behavior and pharmacokinetics, Sci. Rep. 7 (2017) 4131–4141.